Determination of L-X ray absolute emission intensities of ^{238}Pu, ^{244}Cm, ^{237}Np and ^{233}Pa radionuclides using a metallic magnetic calorimeter

Riham Mariam, Matias Rodrigues, Martin Loidl, Sylvie Pierre, Valérie Lourenço

▶ **To cite this version:**

Riham Mariam, Matias Rodrigues, Martin Loidl, Sylvie Pierre, Valérie Lourenço. Determination of L-X ray absolute emission intensities of ^{238}Pu, ^{244}Cm, ^{237}Np and ^{233}Pa radionuclides using a metallic magnetic calorimeter. Spectrochimica Acta Part B: Atomic Spectroscopy, 2022, 187, pp.106331. 10.1016/j.sab.2021.106331 . hal-03554683

HAL Id: hal-03554683
https://hal.science/hal-03554683

Submitted on 3 Feb 2022

HAL is a multi-disciplinary open access archive for the deposit and dissemination of scientific research documents, whether they are published or not. The documents may come from teaching and research institutions in France or abroad, or from public or private research centers.

L'archive ouverte pluridisciplinaire **HAL**, est destinée au dépôt et à la diffusion de documents scientifiques de niveau recherche, publiés ou non, émanant des établissements d'enseignement et de recherche français ou étrangers, des laboratoires publics ou privés.

Determination of L-X ray absolute emission intensities of ^{238}Pu, ^{244}Cm, ^{237}Np and ^{233}Pa radionuclides using a Metallic Magnetic Calorimeter

Riham Mariam[1,2], Matias Rodrigues[1*], Martin Loidl[1], Sylvie Pierre[1] and Valérie Lourenço[1]

[1] Université Paris-Saclay, CEA, List, Laboratoire National Henri Becquerel (LNE-LNHB), F-91120 Palaiseau, France
[2]Present address: Université Paris-Saclay, CNRS/IN2P3, IJCLab, 91405 Orsay, France

* Corresponding author: matias.rodrigues@cea.fr

Abstract

Energy dispersive photon spectrometry is a common analysis technique to quantify radionuclides present in a sample, the analysis is based on the knowledge of the photon emission intensities specific to each radionuclide. Among them, actinides have in general intense emission of L X-rays during the decay. However, their emission intensities are not well known and not detailed in the nuclear and atomic data tables due to the complexity of their spectra that cannot be resolved by conventional semiconductor spectrometers. Using a dedicated high energy resolution cryogenic detector, based on metallic magnetic calorimeter sensor technology, the L X-ray spectra of the decays of ^{238}Pu(α) → ^{234}U, ^{244}Cm(α) → ^{240}Pu, ^{237}Np(α) → ^{233}Pa and ^{233}Pa(β^-) → ^{233}U were measured with an energy resolution between 23 eV and 43 eV (full width at half maximum) given access to an unprecedented level of detail.
Moreover, the detector was conceived to provide a quasi-constant efficiency in the energy range of the L X-rays, minimizing the uncertainty for relative L X-ray emission intensities. Prior to the measurements, the full energy peak efficiency was carefully characterized, which enabled the determination of absolute emission intensities, with an uncertainty of the order of 1%. Some corrections had to be introduced using Monte Carlo simulations, in particular to take into account the surface activity inhomogeneities of the sources. Total and group L X-ray emission intensities are compared with the available data and with the recommended values. In addition, nearly 30 individual L X-ray intensities are presented.

Keywords: Actinides, X-ray spectrometry, Decay data, Cryogenic detectors, Metallic Magnetic Calorimeter,

1. Introduction

Most of the anthropogenic transuranic elements such as plutonium, curium and neptunium are produced by the nuclear energy industry or for nuclear weapons. They have a high toxicity to living organisms and accidental release in the environment would have significant consequences. Therefore, it is necessary to detect and quantify them in many fields and applications: such as the nuclear fuel cycle, the surveillance of non-proliferation treaties, environmental surveys or radioprotection [1–6]. The fractions of the actinides present in a nuclear material provide a variety of information concerning its origin, age and destiny: i.e. isotopic ratios can tell in which type of reactor the material was produced, the burn-up of the nuclear fuel and if the material will be used for civilian or for military applications [3]. Quantitative analysis of actinides is therefore strategic in many applications and various experimental analysis techniques have been developed.

All actinides are radioactive and decay to a daughter nucleus with nuclear and atomic excited states, therefore the decay is accompanied by the emission of many particles: including γ-rays, X-rays and Auger electrons, until the nucleus and the atom attain their fundamental state. These radiations, detected by radiometric techniques, are a useful signature of each nuclide. Among these techniques, photon spectrometry has the advantage to be non-destructive, or at least requires less constraining sample preparation than techniques measuring charged particles (i.e. alpha particles or electrons) [5]. A precise quantification by photon spectrometry needs both well-adapted spectrometers, in terms of detection efficiency, solid angle and energy resolution, and a knowledge of the fundamental parameters relating to the emitted photons: emission intensities, energies and natural line widths. For actinides, there are two energy ranges to be distinguished, above and below 100 keV. Energetic photons can be transmitted through matter to be detected outside of these dense materials, hence the region above 100 keV is generally used for non-destructive analysis of raw nuclear material. However, the emission intensities above 100 keV are generally low, so the materials to be analyzed must contain high concentrations of actinides. Conversely, at low energy, the emission intensities are larger, but the photons are strongly absorbed. Consequently, the low energy region allows the study of weakly active traces on surfaces or in materials with low density, such as liquids or biological tissues, this energy range therefore concerns mainly environmental and biological applications [7,8].

Although the L X-rays are intense compared to the γ-rays, the intensities of individual X-ray transitions at a specific energy are not known; at best only L X-ray group intensities and few individual intense transitions are given. In the databases, the recommended L X-ray emission intensities are evaluated from the different published measurements [9], or, if the measurements are inconsistent or do not exist, the evaluation is based on calculations using atomic and nuclear fundamental parameters [10,11]. Experimentally, the incomplete emission intensity data and their large uncertainties arise from two difficulties. Firstly, the L X-ray spectra are complex since photons arising from several tens of transitions are emitted in a narrow energy range between 10 keV and 25 keV. The energy resolution of semiconductor detectors is insufficient to separate the main transitions. Typically, high purity germanium (HPGe) detectors have an energy resolution of 240 eV full width at half-maximum (FWHM) in this energy range and they can at best distinguish the L groups[1] separated by at least a few keV. The second difficulty is given by the detection efficiency of Si(Li) or HPGe detectors that varies significantly (> 10%) in this low energy range and where not many radionuclides exist for suitable efficiency calibration. In particular, for HPGe detectors, the Ge K-edge discontinuity at 11 keV makes the calibration of the efficiency problematic [12,13].

As is common in the evaluations, the emission intensities of L X-rays can be calculated with nuclear and atomic fundamental parameters (FPs). These parameters are related to each process of the nuclear decay and subsequent atomic relaxation processes. The X-rays are emitted during the atomic rearrangement after the creation of a vacancy in an electron shell. Radioactive decays of actinides produce these vacancies by shake-off, shake-up, electron capture or internal conversion (IC) of a gamma-transition. For the present study, it is only the latter process that produce intense L X-ray emissions, i.e. > 1%. Therefore, for calculating the L X-ray emission probabilities, the primary vacancy distribution is calculated using the γ-transition probabilities and partial internal conversion coefficients (ICC). The K primary vacancies are redistributed from the K to the L shell by X-ray and Auger transitions and the L primary vacancies are redistributed between subshells by Coster Kronig (CK) transitions. The rearranged distribution is calculated using the K-ray, the Auger and the CK transition probabilities. Finally the fluorescence yield and the emission rates are required to calculate the X-ray emission intensities. Therefore, at least five FPs are needed, and some of them have large relative uncertainties, in particular the CK transitions probabilities [14]. Some other parameters cannot be calculated with confidence, for example the ICCs for anomalous γ transitions [15]. Most of the FPs are old, as they were calculated in the 1970s and 1980s, have no uncertainties. In addition, they are based on some basic assumptions i.e. singly ionized elements, even if after the rearrangement through Auger and CK transitions, the atom is multiple ionized, and the proportion of L X-ray emitted from the atom with a spectator vacancy is important.

Precise measurements are therefore necessary; this is why, in the framework of ionizing radiation metrology, we proposed to measure the absolute individual L X-ray emission intensities for different actinides, in order to improve actinide decay data. To provide precise measurements, it is essential to use a spectrometer with a high energy-resolution to separate most of the X-ray lines, and with a well-characterized detection efficiency. The energy resolution of semiconductor spectrometers being intrinsically limited by the Fano factor, spectrometers based on a different physical principle of detection must be used. In this work, a thermal cryogenic detector was developed to measure high energy resolution L-X-ray spectra emitted by

[1] These groups correspond to those defined by the Siegbahn notation in separate energy ranges, namely Lα, Lη, Lβ and Lγ

the decays of ^{238}Pu(α) → ^{234}U, ^{244}Cm(α) → ^{238}Pu, ^{237}Np(α) → ^{233}Pa and ^{233}Pa(β^-) → ^{233}U.

2. Experimental set-up

2.1 The Metallic Magnetic Calorimeter

Thermal cryogenic detectors measure the deposited energy by a particle as a temperature rise. They have demonstrated resolving powers greater than one thousand and energy resolutions more than one order of magnitude better than semiconductor detectors [16]. In this work, we used Metallic Magnetic Calorimeters (MMC) [17]. An MMC consists of an absorber (usually gold) strongly thermally coupled to a paramagnetic thermal sensor made of Au:Er or Ag:Er, with typical erbium concentrations of a few 100 ppm. In a weak magnetic field, the sensor magnetization $M(T)$ is highly dependent on the temperature. This sensor acts as a thermometer and measures the temperature variation ΔT of the detector due to the photon energy E deposited in the absorber: $\Delta T = E/C$, where C denotes the heat capacity of the detector. The sensor is magnetically coupled with a DC superconducting quantum interference device (SQUID) via a superconducting flux transformer consisting of a pick-up coil and an input coil (figure 1.a).

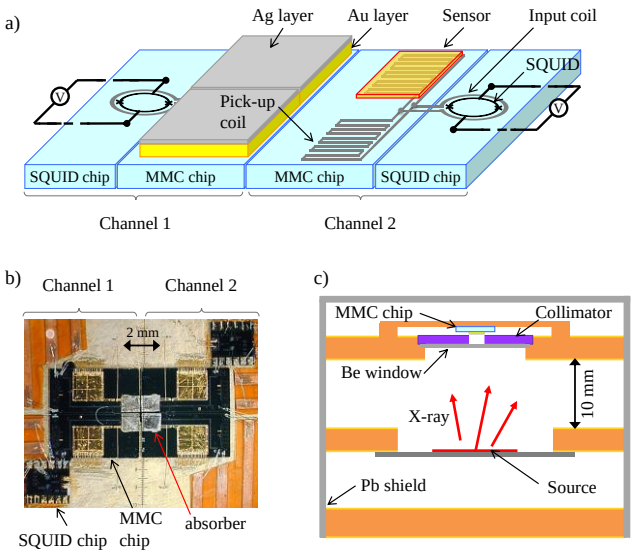

Figure 1. a) Scheme of the MMC SMX3 with its four pixels and their read-out[2] (not to scale). To show a sensor and a pick-up coil under the absorbers, the two pixels of the channel 2 (right) are removed. Each pixel is composed of a stack of a meander-shaped pick-up coil, a gold-erbium sensor layer and a gold-silver bilayer absorber. b) Photo of the MMC SMX3. c) Scheme of the set-up with the MMC, the W collimator, the Be window and the radioactive source.

[2] MMC chips were designed and produced by C. Enss' group at Kirchhoff-Institute for Physics, Heidelberg University.

Therefore, the sensor magnetization variation induces a magnetic flux variation in the SQUID which converts it to a voltage change. The detector returns to its equilibrium temperature, imposed by a thermal bath at temperature T_0, through a weak thermal link. Each absorbed particle produces a pulse proportional to the deposited energy, with a decay time constant $\tau = C/G$, where G is the thermal conductance of the link between the detector and the thermal bath.

The signal-to-noise ratio (SNR) of cryogenic detectors is increased by decreasing the temperature, because the absorber heat capacity decreases with T_0 leading to larger pulse heights ($\Delta T = E/C$). In addition, the fundamental noise limit of thermal cryogenic detectors is the thermodynamical fluctuation noise with a standard deviation proportional to $\left(T_0^2 \cdot C(T)\right)^{1/2}$ [17]. Therefore, at very low temperatures high energy resolutions are achievable. For MMCs, the SQUID read-out electronics has a non-negligible contribution to the SNR and the energy resolution, it dominates the white noise component and has to be considered.

For photon spectrometry applications, a compromise must be found between energy resolution, detection efficiency and maximum count rate capability when conceiving and optimizing the detector parameters [18]. We have developed a 4-pixel MMC detector called SMX3 (figure 1.a and 1.b). The compromise for an MMC dedicated and optimized to photon spectrometry below 25 keV, leads to an energy resolution of 25 eV (FWHM), a count rate capability of about 10 s^{-1}, a detector area of 4 mm² and an intrinsic efficiency > 99% [18]. Such a large intrinsic efficiency is not possible with Au absorbers due to the escapes of the Au L X-ray photons which introduce three discontinuities that are difficult to characterize (figure 2). Adding an Ag layer on top of the Au reabsorbs these photons. Bi-layer absorbers made of gold and silver were used to provide an intrinsic efficiency > 99% between 10 keV and 25 keV, minimizing the efficiency correction. The thicknesses were optimized by Monte Carlo simulations [19].

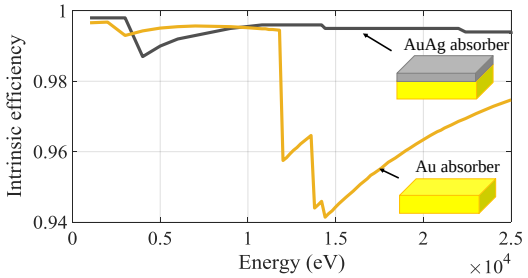

Figure 2. Intrinsic detection efficiencies obtained by Monte Carlo simulations valid for any bi-layer absorbers with thicknesses

of Au ≥ 50 µm and Ag ≥ 16 µm, and for any Au absorbers with thicknesses ≥ 70 µm.

Each absorber has an area of about 1 mm² and is thermally coupled with a planar Au:Er sensor, itself magnetically coupled to a meander shaped pick-up coil [20]. A closed superconducting circuit of two parallel planar meander-shaped pick-up coils is connected in parallel to the input coil of a VC1A SQUID[3], forming the flux transformer (figure 1.a and 1.b).

Therefore two pixels are read by a single SQUID channel and each pixel can be distinguished by the pulse polarity, positive or negative, as the two pick-up coils form a gradiometer with respect to the SQUID input coil. A permanent current of about 60 mA circulates in the closed superconducting circuit formed by the two meanders, in order to create the weak magnetic field of few mT in the paramagnetic sensors necessary for their operation.

The two SQUIDs of the four pixels are biased and are read out by XXF-1 SQUID Electronics[4]. The electronics output voltages are low-pass filtered and amplified by SR560 Low Noise Preamplifiers, and recorded on a hard disk using an Innovative Integration P25M PCI Express digitizer card. At a distance of about 0.48 mm from the absorbers, a 1 mm thick tungsten collimator with a diameter of 1.8 mm defines the solid angle between the source and the 4 pixels (figure 1.c). The latter ones cover 95% of the surface of the collimator hole. Placed on the collimator, a 43 µm thick Be window is used to absorb the alpha particles and the electrons emitted during the decay of the radionuclides. The source is placed at a distance of 15 mm from the collimator, i.e. at very low temperature, about 10 mK, in the same vacuum as the MMC. Thus, between the source and the detector, the L X-ray intensities are only weakly attenuated by the Be window.

Using this detector array of 4 pixels, the photon emission intensity at a given energy E is determined from the energy spectrum by:

$$I(E) = \sum_{i=1}^{2}\sum_{j=1}^{2} \frac{\Omega_{i,j} \cdot N_{i,j}(E)}{4\pi \cdot A(t) \cdot \epsilon_{i,j}(E) \cdot \Delta t_i} \qquad (1)$$

where the index i designates one of the two SQUID channels and the index j one of the two pixels of a given channel,
Δt_i is the live time of the channel i. The pixels of each channel have the same live time,
$N_{i,j}$ is the number of counts in the full energy peak (FEP) of each individual spectrum of the pixel i,j at the energy E,
$\Omega_{i,j}$ is the solid angle between the pixel i,j and the source,
A is the source activity at the time t,
$\epsilon_{i,j}(E)$ is the intrinsic FEP efficiency of the pixel i,j.

Since the efficiency was calibrated globally over the 4 pixels by summing the individual spectra, the equation can be simplified to:

$$I(E) \approx \frac{1}{A(t)\cdot\epsilon(E)\cdot\overline{\Delta t}} \cdot \sum_{i=1}^{2}\sum_{j=1}^{2} N_{i,j}(E) \qquad (2)$$

where ϵ is the mean FEP efficiency of the 4-pixel MMC at a given energy,
$\overline{\Delta t}$ is the mean of the live times Δt_i of the channels.

This approximation is valid when the intrinsic efficiency, the live time and the solid angle between pixels are close. In the present case, it leads to a negligible difference smaller than 0.1%.

2.2 Full energy peak efficiency calibration

Following equations 1 and 2, precise knowledge of the FEP efficiency ϵ is necessary. In general, many standard sources are needed to calibrate accurately the efficiency as a function of energy [21]. For the SMX3 detector, each standard source would require a measurement of more than one week. In order to minimize the time involved and the cost of this method, the efficiency was calibrated by combining the measurement of only one standard source of ^{241}Am with Monte-Carlo (MC) simulations [22]. The measurement with ^{241}Am provided some experimental efficiency values used as references to generate the most appropriate MC simulation meta-geometry giving the best agreement between the simulated and the experimental efficiencies. Two experimental FEP efficiency values used as references were determined from the emission intensities of the 59.54 keV γ-ray line and the Np Lβ X-ray group between 16 keV and 19 keV [9]. An initial geometry was measured using two dimensional metrology systems, a Mitutoyo Quick Vision system for measuring areas and a measuring column (Roch) for distances and thicknesses. Therefore, the critical dimensions affecting the FEP efficiency, (i.e. the thicknesses of the absorber layers, the lateral position of the collimator and the distance between source and collimator) were derived by minimizing the deviation between the simulated and experimental efficiency. Once the meta-geometry was found, the FEP detection efficiency was simulated at different energies, and interpolated to have a continuous curve between 0 and 100 keV (upper part of figure 3). Moreover, it is possible to calculate the efficiency transfer for various source geometries [23].

The uncertainty of the efficiency can be discussed considering three energy ranges (lower part of figure 3). Above 25.5 keV, i.e. the K edge of silver, the uncertainty is dominated by our knowledge of the absorber layer thicknesses t_{Au} = 54.11 (9) µm and t_{Ag} = 16.06 (40) µm, respectively for the Au and Ag layers. Their uncertainties are

[3] Supracon® AG http://www.supracon.com
[4] Magnicon GmbH http://www.magnicon.com

linked to the uncertainty of the 59.54 keV γ-ray intensity of ^{241}Am (35.92 (17) %) [9]. The propagation of the absorber thickness uncertainty to the efficiency was determined using MC simulations by varying the layer thicknesses according to their uncertainty.

Below 25.5 keV, the uncertainties of the absorber thicknesses do not contribute because the intrinsic efficiency of the absorbers is practically constant and close to one. Between 6 keV and 25.5 keV, the uncertainty is dominated by the contribution of the distance between the source and the absorbers, itself established using the ^{241}Am intensity of the Lβ X-ray group (18.58 (13) %) [9]. This distance in the MC geometry is 15.98 (16) mm, and is consistent with that measured by the Roch column, 16.059 (6) mm. Below 6 keV, the uncertainty is a combination of the uncertainties of the Lβ intensity and the transmission through the Be window. The latter one is given by uncertainty of the linear attenuation coefficient of Be and by the uncertainty of the Be thickness, 42.97 (7) µm [24]. It should be noted that the variation of the efficiency is only 0.3% between 10 keV and 23 keV, i.e. the L X-ray energy range of actinides.

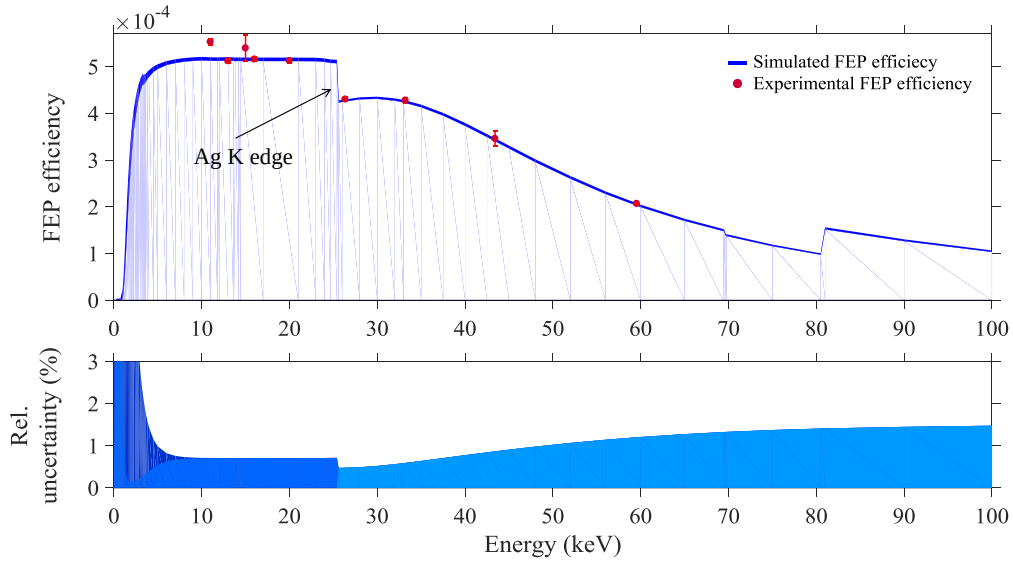

Figure 3. Top, FEP detection efficiency as a function of energy obtained experimentally with an ^{241}Am source (red dots) and by Monte Carlo simulations (blue line). The thickness of the line corresponds to one standard deviation. Bottom, the relative uncertainty of the FEP efficiency and its relative contributions: dark blue, contribution from the transmission through the Be window; blue, contribution from the Np Lβ X-ray intensity, and light blue contribution from the 59.54 keV γ-ray intensity.

2.3 Preparation of the radioactive sources

The three sources of ^{238}Pu, ^{244}Cm and ^{237}Np with an active diameter of 12 mm were prepared in our laboratory by electro-precipitation on stainless steel planchets.

Protactinium-233 is in equilibrium with ^{233}Np, therefore the two actinides have the same activity. The electro-precipitation technique was preferred because it was expected to provide homogeneous and thin deposits. Curium-244 and ^{238}Pu sources have a deposit thickness lower than 0.1 nm, but the ^{237}Np source had a far more significant thickness of 57 nm of NpO_2 due to its long half-life, therefore its self-absorption has been considered. While the surface activity distribution was expected to be homogeneous, source autoradiographies revealed it was not the case. As we will show later, source inhomogeneities have to be taken into account when measuring the absolute emission intensities with the present detection geometry. For each nuclide, the source activity was chosen to obtain a count rate of about 5 s^{-1}. The actual activities of the sources were measured with a low uncertainty using defined solid angle alpha counting (DSAC). DSAC is a primary activity standardization method. The activity of the alpha emitting radionuclide is determined by correcting the observed count rate by the geometry factor, $\Omega/4\pi$. The latter is calculated from accurate distance measurements of the detection geometry [25].

At the measurement dates the activities were 57.82 (10) kBq, 69.91 (18) kBq and 1.856 (6) kBq respectively for the ^{238}Pu, ^{244}Cm and ^{237}Np/^{233}Pa sources. The three sources were mounted successively in front of the detector and the set-up was cooled to the operating temperature in a dilution refrigerator. The detector temperature was not regulated and was imposed by the base temperature of the cryostat comprised between 11 and 13 mK. Each measurement lasted for two weeks in order to record several million counts in the L X-ray region.

These sources have a larger diameter than the standard ^{241}Am source used for the efficiency calibration with a diameter of 8 mm. To take into account this difference, an efficiency transfer by MC simulations was performed using the meta-geometry established in 2.2.

3 Recording and spectrum processing

3.1 Signal and data processing

In the following section, the signal and the data processing to obtain the spectra will be discussed, the aims being to get energy peaks with the best energy resolution and with a shape as close as possible to a Gaussian, and to determine the live time.

The signal outputs of the two-channel SQUID electronics were digitized with 16-bit resolution and 250 kHz sampling frequency, and the data were stored continuously on an SSD disk. We choose offline analysis in order to adapt the signal processing to the various experimental conditions of each measurement depending on the base temperature, the temperature fluctuations, the count rate or the noise level. Above all, the offline analysis allows each step of the signal and data processing to be verified. In particular, it was crucial for these quantitative measurements to check the live time determination and the pile-up rejections. The data processing is divided into the following steps:

1- Detection of the pulses with positive and negative triggers in the filtered data stream using a strong band pass filter, recording of the time stamps of the start and the end times (t_{start} and t_{end}) of the triggered events.
2- Construction of the optimal filter with a noise template and a pulse template [26].
3- Application of an extendable dead time [22,27]. Determination of the live time Δt. Rejection of any pile-up on the pulse baseline[5].
   The dead time window W_{dt} is adjusted for each trigger event, considering that the pulse duration above the trigger is proportional to its amplitude. W_{dt} is set by:

$$W_{dt} = f_{dt} \cdot (t_{end} - t_{start}) + W/2$$

   where f_{dt} is a factor ensuring that the pulse is returned to the baseline after the duration W_{dt}, and $W/2$ is a safety delay so that the baseline of the next pulse does not fall into the decay time of the current event. Typical dead times were about 10%.
4- Analysis of the non-rejected pulses. Determination of the pulse height after optimal filtering. Determination of other parameters needed for pile-up rejection such as time position of the pulse maximum after the triggering (t_{max}) and the χ^2 from the fit between the pulse template and the pulse (χ^2_{pulse}).
5- Rejection of the pile-up on the pulse decay based on cuts on the parameters t_{max} and χ^2_{pulse}.
6- Rejection of the pulses during the liquid helium filling of the cryostat, corresponding to strong temperature variation and large χ^2_{pulse}.
7- Correction of the live time Δt due to the pulse rejections in 5 and 6.
8- Correction of the pulse height variation due to the temperature drift using a spline function obtained by fitting the drift of a reference line as a function of time.

Steps 1, 3, 6 and 7 are performed for each channel, while the steps 2, 4, 5 and 8 are done for each pixel.

Special attention has been paid to the live time determination and the pile-up rejection that can lead to systematic errors when measuring absolute emission intensities (equation 2). We can distinguish two types of pile-up: the first one occurs when another pulse falls into the pulse baseline, the second one occurs when another pulse falls into the rise or fall of the pulse. The extended dead time rejects the first type (step 3) and the second type of pile-up is rejected by step 5. However, step 5 rejects pulses in the live time, therefore after step 5, the live time Δt must be corrected in step 7 by the probability P_0 using the Poisson law, i.e. the probability to have no pulse within one half of the pulse window duration W (rise and fall)[5] :

$$P_0 = exp\left(-\frac{Cr \cdot W}{2}\right) \qquad (3)$$

where Cr is the count rate per SQUID channel (positive and negative pulses) before the pile-up rejection of step 5.

Pile-up with a pulse falling into the rise time of the pulse cannot by rejected by step 5, however the probability of this situation is very low, less than 0.05%.

The live time determination and the signal processing were checked using a digital pulser method. The method consists in digitally adding pulses having the shape of the template pulse into the experimental raw data stream. The pulses are randomly distributed with a known count rate. The same steps of signal and data processing described above were applied to obtain the energy spectrum. The live time

[5] An analyzed pulse has a window W of 8192 samples, i.e. a duration of 32.8 ms. The first half of the 8192 samples is defined as the pulse baseline, i.e. before the start timestamp, and the second half comprise the rise and the fall of the pulse.

determined from the extendable dead time after the rejection correction (equation 3) is consistent with the live time from the pulser within statistical uncertainties, about 0.3%.

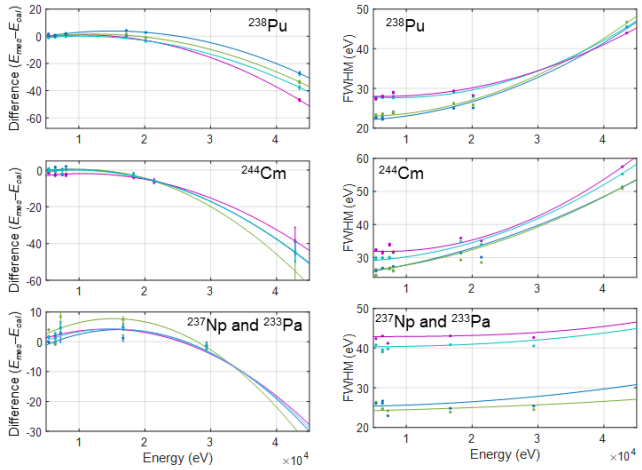

Figure 4. Left panels show the difference between the measured energies (E_{mes}) before the non-linear correction and the energies used for the calibration (E_{cal}). The curves are the polynomial functions (lines) used to linearize the energy responses of the different pixels. Right panels shows the polynomial functions P_{FWHM} (lines) used to homogenize the energy resolution FWHM of the four pixels. The dots are the experimental data. The four colors represent the four pixels.

The signal processing for the two channels provides the pulse energies of the four pixels. However, the pixels have different energy resolutions and non-linearities due to slightly different thermodynamic quantities of the sensors and absorbers. Before summing the energy histograms of the different pixels, it is therefore necessary to introduce some corrections to the pulse energies, since the simple sum of Gaussian functions, with different arithmetic means and/or different variances, does not provide a Gaussian. The response of MMCs is known to be very linear in energy and therefore the "SMX3" detector has a maximum non-linearity, i.e. deviation of measured line energies from tabulated values, of only about 40 eV between 0 keV and 50 keV (figure 4). Nevertheless, the non-linearity is significant compared to the energy resolution and has to be individually corrected for each pixel. Ten calibration lines were used to derive a quadratic polynomial and to correct the pulse energies from the non-linearity. The calibration lines are the particle-induced K X-ray lines from the stainless steel source backing (Fe, Cr and Ni), the most intense γ-ray lines below 100 keV and the intense Lγ_1 (L_2-N_4) and Lβ_1 (L_2-M_4) X-ray lines from the measured actinides. After correction, the standard deviation between the calibration energies and the corrected energies is less than 2 eV.

In addition, the energy resolutions of the individual pixels have to be made equal to the poorest resolution of the four pixels. The energy resolution increases slightly with the energy, a quadratic polynomial P_{FWHM} describes this dependence (figure 4).

3.2 Spectrum processing

After summing the corrected energy spectra of the four pixels the resulting spectrum was processed using the software Colegram [28]. Each L X-ray was fitted by a Voigt function, i.e. the convolution of a Gaussian, related to the instrument line shape, and a Lorentzian, related to the atomic transition natural line width. The Gaussian widths have been fixed according to the polynomial P_{FWHM}. The Lorentzian widths were set using the database of Campbell [29], and for ^{238}Pu and ^{233}Pa (X-rays emitted by uranium) the values from Hoszowska [30] were used. In some very complex spectrum regions and/or portions of the spectra with weak peaks, the energies and/or the amplitudes were fixed. The energies were taken from the recommended database by Porter [31] and the relative intensities were taken from the rates calculated by Scofield [32].

If the X-ray transitions are diagram lines, i.e. transitions occurring in an atom with a single vacancy state, each L X-ray peak could be fitted using a single Voigt function. However many processes can lead to atoms with multiple vacancy states followed by X-ray transitions with shifted energy compared with diagram lines, the so-called satellite lines. In the present cases, the dominant process of multiple vacancy production is related to the Auger and CK transitions. After such a transition the atom has at least two vacancies. The CK transitions, L_1L_3X or L_2L_3X, have a high probability to occur when there is a vacancy in L_1 or L_2 [33], leading to an additional vacancy in an outer shell X = M, N, O, P, Q. Therefore, the L_3 X-ray satellites are intense when the number of primary vacancies in L_1 or L_2 is high; resulting in some spectrum structures appearing either as a right tail or as one or several additional peaks shifted to higher energies relative to the diagram line. Satellite peak shapes are complex, related to tens of different possible transitions and they are different for each L_3-X_j transition (X_j designating the implied outer (sub-)shell) [34]. The L_3 X-ray satellite structures were fitted using up to three Voigt functions, see for example for Lα_1 (L_3-M_5) and L$\beta_{2,15}$ (L_3-$N_{4,5}$) in figure 9. Moreover, for different actinides, the intensities of the satellites are also different, because of different partial IC coefficients. If the α_{L3} partial IC coefficients dominate the α_L coefficients, the L_3 X-ray peaks will be mainly composed of diagram transitions while if α_{L1} and α_{L2} dominate, L_3 X-ray peaks will be mainly composed of satellites transitions. As shown in figures 9, the L_3 X-ray spectrum of ^{244}Cm(α) → ^{240}Pu has intense satellites, while in figures 8 they are weak for ^{238}Pu(α) → ^{234}U.

The other processes of satellite production in the L X-ray spectrum are the Auger transitions filling a K vacancy, i.e. KLX and KLL transitions. The KLL Auger transitions produce hypersattellites that are X-ray transitions occurring when the atom has more than one vacancy in the same shell. For ^{238}Pu and ^{244}Cm there are less than 0.1 K vacancies per 100 decays, therefore this process is negligible. For ^{237}Np and ^{233}Pa, there are respectively 5.5 and 31.7 K vacancies per 100 decays, but only 3% of them are followed by a K Auger transition, leading to weak satellite intensities. Among these satellites, only one weak peak in the spectrum of ^{237}Np/^{233}Pa at 13 948 eV could be assigned to a Lα_l hypersatellite of uranium (figure 10). The energy shift (330 eV) is close to that measured by Imanishi [35], 230 (60) eV, but this peak could also be due to some auto-fluorescence of Np at 13 944 eV. Without a clear presence and because of their small intensities, these satellites from K Auger transitions were ignored.

For ^{238}Pu, ^{244}Pu and ^{233}Pa, the L_1-L_3 X-ray transition around 4.5 keV was clearly visible and was fitted with a Voigt function (figures 8, 9 and 10). The presence of a nearly constant background is fitted using one-step functions or an exponential function (figures 8, 9 and 10).

The uncertainty resulting from the fitting procedure has two components, the statistical uncertainty and the systematic uncertainty. The latter depends on some assumptions of the physical model used for the fit. The systematic uncertainty was evaluated from the results of different fitting procedures for different regions of interest, with different background modeling, or with free Lorentzian widths for the main X-ray peaks.

3.3 Correction for source inhomogeneity

The electro-precipitated sources were expected to have a homogeneous activity distribution. However, auto-radiographies show important inhomogeneities, the ^{238}Pu source is the worst case amongst the three sources (figure 5). Such inhomogeneities can lead to significant bias in the assumed detection efficiency if we do not take them into account. Indeed, given the distance of 15 mm between the source and the collimator, the source is large (12 mm diameter) compared to the collimator hole (1.8 mm diameter) and is hence not seen as a point source by the detector. Therefore, the efficiency depends on the geometrical efficiency, which in turn varies with the position where a photon is emitted. For photons emitted at the edge, the solid angle of the collimator is 10% lower than for photons emitted at the center. Moreover, the collimator thickness of 1 mm increases this effect, the collimator acts as two diaphragms and masks part of the photons emitted outside a radius of 1 mm from the center [25].

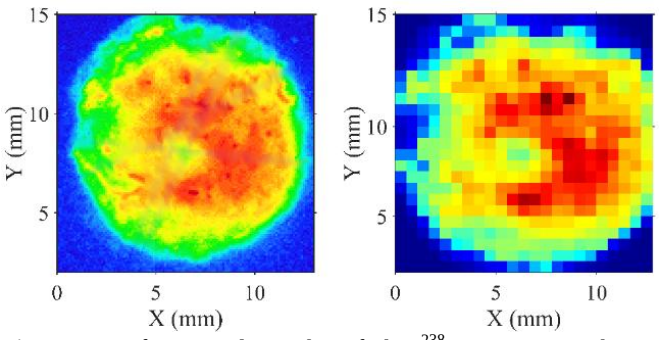

Figure 5. Left, autoradiography of the ^{238}Pu source. Right, 2-dimensional distribution of the source activity $A_{x,y}$ after reduction to 24x24 pixels.

To correct the effect of the source activity distribution, the factor C_{inhomo} has been introduced in equation 2:

$$I(E) \approx \frac{1}{C_{inhomo} \cdot A(t) \cdot \epsilon(E) \cdot \overline{\Delta t}} \cdot \sum_{i=1}^{2}\sum_{j=1}^{2} N_{i,j}(E) \qquad (4)$$

The factor C_{inhomo} is calculated from equation 5 using the 2-dimensional distribution of the activity $A_{x,y}$ (figure 5) and the 2-dimensional map of FEP efficiency $\epsilon_{x,y}$ over the source area (figure 6) [36]:

$$\sum_{x=0}^{n-1}\sum_{y=0}^{n-1} A_{x,y}(t) \cdot \epsilon_{x,y}(E) = C_{inhomo} \cdot A(t) \cdot \epsilon(E) \qquad (5)$$

with $A(t) = \sum_{x=0}^{n-1}\sum_{y=0}^{n-1} A_{x,y}(t)$,

and $\epsilon(E) = \sum_{x=0}^{n-1}\sum_{y=0}^{n-1} \epsilon_{x,y}(E)$

$A_{x,y}$ is extracted from the autoradiography in the form of a 24×24 array (figure 5); each element (x, y) has an area of 0.5×0.5 mm². For each element (x, y), the efficiency $\epsilon_{x,y}(E)$ was calculated by Monte Carlo simulation. Figure 6 shows the simulated efficiency map, we can notice the relatively large dependence of the efficiency on the (x, y) position.

The correction factors C_{inhomo} are 1.0306 (37), 0.970 (12) and 0.984 (7) respectively for the ^{238}Pu, ^{244}Cm and ^{237}Np/^{233}Pa sources. The uncertainty of C_{inhomo} was calculated considering the uncertainty contributions from the autoradiography resolution, the azimuthal orientation of the source and the background due to scattering in the autoradiography plate.

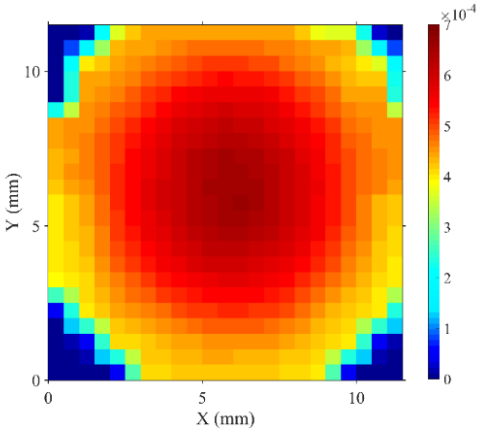

Figure 6. 2-dimensional map of the efficiency $\epsilon_{x,y}$ for isotropic emission of 15 keV photons calculated by Monte Carlo simulation covering a disk of 12 mm diameter.

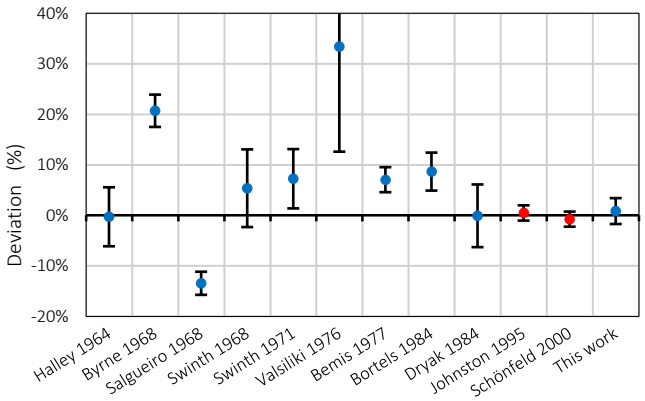

Figure 7. Deviations of the published total L X-ray emission intensities with the recommended value (10.63 (8)%) for ^{238}Pu, with a coverage factor k = 2 [9,39]. Blue points are experimental data, red points are calculated data. The calculated intensities do not have associated uncertainties, in this case, the uncertainty shown is recommended value uncertainty.

4 Photon emission intensities

For each radionuclide, the Lα, Lη, Lβ, and the Lγ intensities, as well as the total L X-ray intensity, are compared with the published experimental data and with the recommended data of the Decay Data Evaluation Project (DDEP) [9,37] and with the calculated values from the EMISSION based on atomic and nuclear FPs [10,11].

4.1 L X-ray spectrum of ^{234}U from the decay of ^{238}Pu

Plutonium-238 decays by α-particle emission to the radionuclide ^{234}U with a relatively simple decay scheme, 71.04 (6) % of the decays populate the ground state and 28.85 (6) % the 43.5 keV level. The L X-rays are mainly produced by the strong internal conversion of the γ–ray which depopulates this level. Plutonium-238 and ^{234}U have half-lives of 87.74 (3) a and 2.455 (6) × 10^5 a respectively [9]. Plutonium-238 being one of the few actinides for which:

- total L X-ray intensity have numerous measurements, although there are discrepant (figure 7),
- a good agreement between the calculations and the recommended value is observed (figure 7),
- there are two measurements of individual emission intensities were published [38,39].

It is therefore a radionuclide that allows the present work, which introduced the use of a cryogenic detector, to be compared with the numerous published data.

The recommended intensity, 10.63 (8) %, is the value measured by Johnston [9,39], because it has a low uncertainty and it is in agreement with Dryak (10.62 (32) %) [38] and the calculated value of 10.55 (25) % [11]. In this work, the measured total L X-ray intensity is 10.72 (11) %, in good agreement with the recommended and calculated values as presented in table 1 and in figure 7.

The presently measured L X-ray groups are listed in table 2 and are in good agreement with those recommended and calculated. The recommended values of the L X-ray groups were evaluated from four measurements and renormalized by the recommended total L X-ray intensity [9]. From the results of the spectrum processed as presented in Figure 8, table 3 presents 29 absolute and relative emission intensities.

The uncertainties on the absolute emission intensities result from the contributions of: 1. the uncertainty from the source inhomogeneity and source positioning, 2. the FEP efficiency, 3. the statistical uncertainty and the spectrum processing uncertainty, 4. the live time and 5. the source activity. The first two contributions are dominant, and the third one can dominate for weak lines in complex regions. The uncertainty for the relative intensities is only given by the contributions of the statistical and the spectrum processing uncertainties.

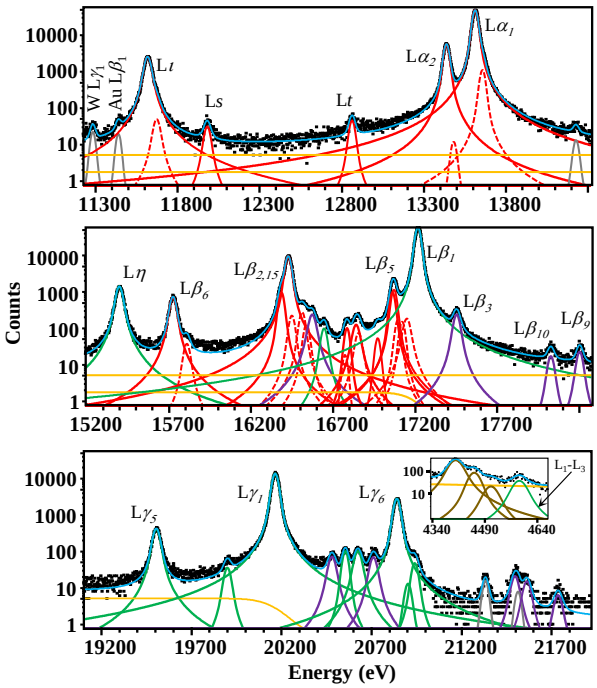

Figure 8. Decay L X-ray spectrum of ^{238}Pu(α) → ^{234}U measured with the MMC SMX3. The black dots are the experimental data, the red, green and purple Voigt functions are respectively the L_3, L_2 and L_1 X-rays. The dashed Voigts are the satellite structures. The grey lines are some fluorescence lines (W Lγ_1 at 11 285 eV and Au Lβ_1 at 11 442 eV) and some escape peaks (at 21 335 eV and 21 508 eV: Ag Kα escapes from the 43 498 eV γ-ray; at 14 234 eV Ag Lα_1 escape from the Lβ_1). The yellow lines are two one-step functions for the background, the total background is the sum of these two functions. The blue line is the resulting total fit. The insert in the lower panel shows the L_1-L_3 X-ray transition nearby some M X-rays (brown lines). The relationship between Siegbahn and UIPAC nomenclature is available in table 3.

Plutonium-238 is one of the few actinides for which many individual L X-ray intensities were determined by more than one measurement: Dryak using HPGe and Si(Li) detectors, and Johnston using an HPGe detector, published about fifteen X-ray intensities [38,39]. Table 4 compares the present results with these values. Surprisingly, although there are peak identification errors and the resolution is insufficient to separate many peaks, the values are in good agreement for most lines, especially with Dryak, even for L*s* and L*t* which have very low intensities. Nevertheless, as the intensities decrease, large differences appear in the Lβ and Lγ regions.

4.2 L X-ray spectrum of ^{240}Pu from the decay of ^{244}Cm

Curium-244, with a half-life of 18.11 (3) a, decays to ^{240}Pu, with a half-life of 6561 (7) a, by α-particle emission, where 76.7 (4) % of the decay populates the ground state and 23.3 (4) % the 42.8 keV excited level; the γ-transition of the latter is highly converted.

The ^{244}Cm activity measured by DSAC is 69.91 (18) kBq, in addition, the presence of 504 (50) Bq of a Pu impurity has been detected, but subsequent alpha spectrometry cannot distinguish between possible ^{239}Pu and ^{240}Pu content. In the measured ^{244}Cm X-ray spectrum, the Pu Lα X-ray lines were detected, if we consider only an impurity of ^{239}Pu, the estimated activity is 808 (18) Bq, while if it is only ^{240}Pu the activity is 337 (8) Bq. Combining the results from alpha and X-ray spectrometry, the impurity is most certainly a mixture of 35% of ^{239}Pu and 65% of ^{240}Pu [8].

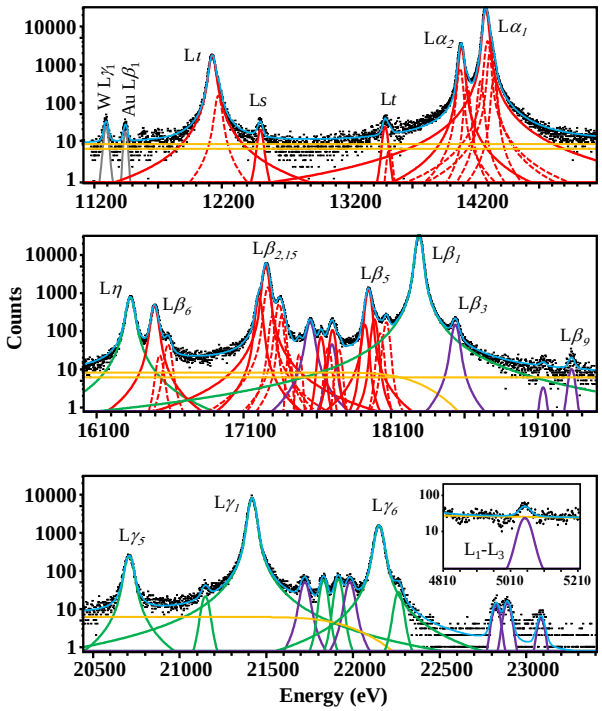

Figure 9. Decay L X-ray spectrum of ^{244}Cm(α) → ^{240}Pu measured with the MMC SMX3. The black dots are the experimental data. The red, green and purple Voigt functions are respectively the L_3, L_2 and L_1 X-rays. The dashed Voigts are the satellite structures. The grey lines are some fluorescence lines (W Lγ_1 at 11 285 eV and Au Lβ_1 at 11 442 eV). The yellow lines are two one-step functions for the background, the total background is the sum of these functions. The blue line is the resulting total fit. The relationship between Siegbahn and UIPAC nomenclature is available in table 3.

To avoid possible interference between the X-rays of Pu and ^{244}Cm, the Pu X-ray spectrum was subtracted using the normalized spectrum for ^{238}Pu previously measured. We have assumed that the normalized L X-ray spectra between Pu isotopes are identical. In reality, from the decay data and the FPs, the L_i X-ray relative intensities are slightly different between these two isotopes but only by 10%, this difference is negligible given the small proportion of impurity. The resulting spectrum is shown in figure 9.

Unlike ^{238}Pu, the L X-rays of ^{244}Cm have been little measured, there being only three measurements of the

absolute total emission intensity: 9.48 (14) %, from Byrne et al. [40], 9.44 (10) % from Bemis et al. [41] and 8.77 (6)% from Johnston and Burns [39]. The latter value is in agreement with the calculated one of 8.92 (23)% chosen as the recommended value [9]. The present measured total L X-ray intensity is 9.08 (16) % in good agreement with the calculated and recommended value; it is also in agreement with the three measurements, but with an expanded uncertainty, i.e. a coverage factor $k = 2$ (table 1).

The present intensities of Lι, Lα, Lη, Lβ and Lγ, are given in table 2, where it can be seen that they agree very well with those calculated by the EMISSION code [11] and agree well with those from Johnston [39]. Twenty-nine L X-ray emission intensities have been measured and are shown in table 3.

4.3 L X-ray spectra of ^{233}Pa and ^{233}U from the decays of ^{237}Np and ^{233}Pa

Neptunium-237, with a half-life of $2.144\,(7) \times 10^6$ a, decays by α-particle emission to ^{233}Pa, which has a relatively short half-life of 26.98 (2) d, and in turn decays to ^{233}U by β^- emission.

The ^{237}Np source activity obtained by DSAC is 1856 (6) Bq, the ^{233}Pa activity cannot be measured precisely and easily, however, considering the two half-lives, the two radionuclides are in secular equilibrium and have the same activity. Compared to ^{238}Pu and ^{244}Cm, both ^{237}Np and ^{233}Pa have much more complicated decay schemes and many levels below 100 keV, whose depopulating γ–transitions are highly converted and hence produce L X-rays with large emission intensities, respectively 59.7 (32) % and 40.6 (11) % [9]. Their L X-rays are emitted in the same energy range, between 10 and 23 keV, thus, the measured spectrum is complex and difficult to process. In addition, this difficulty was enhanced by various experimental constraints:

1. One of the two detector channels had a degraded energy resolution of 43 eV.
2. The spectrum background was higher due to energetic electrons (> 55 keV) going through the Be window and due to Compton scattering of the 312 keV γ-rays.
3. The escape peaks from the two 86.5 keV γ-ray lines fall into the L X-ray energy range.
4. There is self-fluorescence of neptunium in large quantities in the source due to its long half-life. For the latter, the Lα_1 X-ray line of Np can be identified in the spectrum from which one can estimate a negligible contribution of about 0.2% of auto-fluorescence in the L X-ray energy range (figure 10).

In addition, for this measurement we had to take into account the self-absorption in the source. This was done using the NIST XCOM database [42]. The 57 nm of NpO_2 absorbs 0.5% of the 11 keV photons.

For ^{237}Np, 19 X-ray intensities have been determined and are listed in table 5. Using the Scofield calculations [43], we estimated they represent 99.2% of the total L X-ray emission, mainly because the L_1-L_3 X-ray line at 4.8 keV cannot be resolved and detected [43]. Taking into account the fraction of missed X-rays, the measured total L X-ray emission intensity is 56.5 (7) %. It agrees with the recommended value of 59.7 (32) % (table 1), evaluated from three measurements, but with scattered results, explaining the large uncertainty on the recommended value.

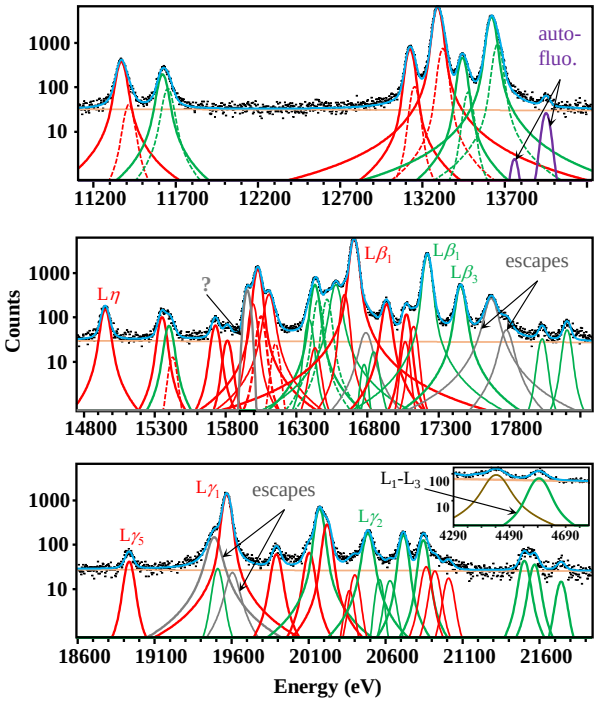

Figure 10. Decay L X-ray spectrum of ^{237}Np(α) → ^{233}Pa and ^{233}Pa(β^-) → ^{233}U measured with the MMC SMX3. The black dots are the experimental data. The red and the green Voigt functions are respectively the ^{237}Np and ^{233}Pa L X-rays. The dashed Voigt functions are the satellite structures. The purple and the orange lines are respectively the auto-fluorescence of Np (or Lα_1 hypersattellites), and the exponential function for the background. The grey Voigts are γ escape peaks (17 673 and 19 486 eV Au Kα escapes from 86 477 eV γ-ray; 17 791 eV and 19 604 eV from the 86 595 eV γ-ray). The blue line is the resulting total fit. The insert in the lower panel shows the L_1-L_3 X-ray transition nearby an M X-ray line (brown line). The relationship between Siegbahn and UIPAC nomenclature is available in table 3.

The lack of precise measurements cannot be compensate by the precise calculations, because they are not consistent with any of the measurements: the EMISSION code gives 50.6 (22) %. This discrepancy might be caused by the complex and unbalanced gamma levels, and by E1 anomalous gamma transitions [15,44]. Between the three measurements, the present value agrees with the 54.8 (21) % obtained by Shchukin (table 1) [9,45]. Even though the

measured L X-ray spectrum of ^{237}Np is in equilibrium with ^{233}Pa, difficult to analyze with HPGe spectrometers, Shchukin and coworkers [45] used a detailed and sophisticated processing of the spectrum, and their result shows relatively good agreement with the current L X-ray group intensities. The present total L X-ray intensity does not agree with the most recent measurement from DeVries et al. [46], of about 62%. Although these authors measured a purified ^{237}Np liquid source, their measurement suffered from a large correction of X-ray self-absorption in the liquid source.

For ^{233}Pa, 24 L X-ray lines have been measured and are listed in table 5, representing 99.8% of the calculated intensities from Scofield [43]. The recommended value for ^{233}Pa is 40.6 (11) % and it is only based on calculations because there is only one suitable measurement, the one from DeVries [46] but with large self-absorption. The other measurements are incomplete and not exploitable, because their spectra cannot be resolved from the ^{237}Np spectrum [45,47]. The present total L X-ray intensity is 38.0 (5) %, consistent with the recommended value, with an extended uncertainty at $k = 2$ (table 1). However the calculations are sensitive to the 28.6-keV γ-ray transition which appears to have incoherent published probabilities [48]. The present L X-ray group intensities of Lι, Lα, Lη, Lβ and Lγ in table 2 are in relatively good agreement with the calculation.

4.4 Comparison with the calculated L-subshell intensity

The individual L X-ray intensities could be measured with the high energy resolution of the MMC, allowing for access to the L_i subshell intensities (i = 1. 2. 3). Indeed, the L_1 and L_2 X-rays are mixed in the Lη, Lβ and Lγ groups (figures 8, 9 and 10). A comparison between experimental and calculated L_i intensities is interesting because these intensities give an indirect picture of gamma transitions, internal conversion coefficients and mixtures of γ transitions. Experimental measurements are indispensable in the presence of abnormal gamma transitions and to balance the admixture of gamma transition multipolarities.

In figure 11, the L_i subshell intensities of ^{238}Pu and ^{244}Cm show good agreement with calculations; while it is not the case for ^{237}Np and ^{233}Pa, showing that their decay schemes, in particular the gamma transition parameters, are not sufficiently well known and consistent. For the four radionuclides, the L_1 intensities have systematically a deviation larger than the uncertainty, although these uncertainties are already large. It shows that the deviation may be caused by the L_1 atomic FPs. i.e. the fluorescence yield ω_1 and/or the CK transition probabilities f_{12} and f_{13}. The EMISSION code uses the atomic FPs from Puri. More recent L_1 FPs were re-evaluated by Campbell [33,49]. Figure 11 shows a much better agreement between the present measurement and the calculations using these FPs.

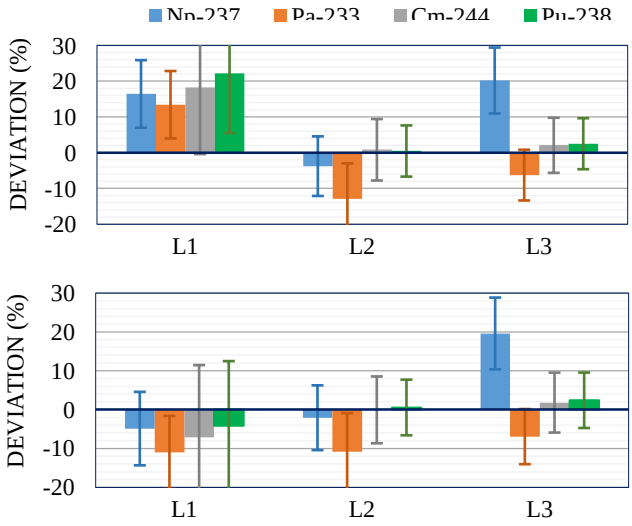

Figure 11. Top, deviations between the present results and calculated L_i emission intensities using the Decay Data Evaluation Project codes and atomic FPs from Puri [10,49]. Bottom, deviations using the atomic FPs evaluated by Campbell [33]. The expanded uncertainties are shown with a coverage factor $k = 2$.

5 Conclusion

For the first time, we have demonstrated that cryogenic detectors are suitable for the measurement of absolute photon emission intensities. The high energy resolution of these detectors is a clear advantage when measuring very complex spectra such as L X-rays of actinides. For the four actinides presently studied, the total L X-ray intensities are in good agreement with the recommended values, for ^{237}Np and ^{233}Pa the present uncertainties are significantly smaller than those of the recommended values. These results validate the experimental approach used in this work, in particular the method used for the FEP efficiency calibration, the signal and data processing, and the spectrum analysis.

The important contribution of this work mainly concerns the intensities of L X-ray groups and the individual X-ray transitions. The instrumental resolution allows, for the first time, to identify and quantify tens of L X-ray transitions for each actinide. It allows a reduction of the associated uncertainties and the possible systematic effects from the spectrum analysis. Amongst the measured L X-ray transitions, we have observed the intense L_3 X-ray satellite structures and taken them into account in the fitting procedure. In addition for three actinides, we have quantified the singular L_1-L_3 X-ray line around 5 keV. Individual L X-ray intensities give access to L_i subshell intensities which are an important parameter to verify the coherence of the decay scheme and of some gamma transition parameters. We have also shown that it is preferable to use the fluorescence yields and the Coster-Kronig transition probabilities from Campbell

[50] rather than those from Puri [49] when calculating X-ray intensities with fundamental parameters.

Currently, the uncertainty of the main X-ray lines is limited by the contribution of the surface activity inhomogeneity of the source. This contribution could be reduced by improving the source preparation, by modifying the detection geometry so that the source is seen as a point source, or by a more precise correction of the source inhomogeneity. For the weak L X-ray lines, the uncertainty is affected by the statistical uncertainty and the systematic effects in the fitting procedure. It can be reduced by improved counting statistics, which would require substantially longer measurement times or larger MMC detector arrays. Such arrays are currently being developed for many applications based on photon spectrometry [16].

Acknowledgment

We thank Giuseppe Lorusso from the National Physical Laboratory, UK, for kindly providing us with the solution of ^{237}Np and ^{233}Pa.

Table 1. Comparison between the total L X-ray emission intensities of ^{238}Pu(α) → ^{234}U per 100 decays obtained in this work with those evaluated, measured or calculated with EMISSION code.

Actinide	This work *I*w (%)	Evaluated or other measured values *I*m (%)		Deviation (*I*w-*I*m)/*I*m (%)	Calculated values *I*c (%) [11]	Deviation (*I*w-*I*c)/*I*c (%)
^{238}Pu	10.72 (11)	10.62 (32) 10.63 (8)	[38] [39]	0.8 (13) 0.9 (32)	10.55 (25)	1.6 (26)
^{244}Cm	9.08 (16)	8.77 (6) 9.44 (10)	[39] [41]	3.5 (20) -3.8 (20)	8.92 (23)	1.8 (32)
^{237}Np	56.5 (7)	59.7 (32) 54.8 (21)	[9] [45]	-5 (5) 3.1 (42)	50.60 (22)	11.7 (15)
^{233}Pa	38.0 (5)	-	-	-	40.6 (11)	-6.5 (28)

Table 2. Comparison and deviations between the total L X-ray emission intensities per 100 decays obtained in this work with those evaluated, measured or calculated with EMISSION code.

	$^{238}Pu(\alpha) \rightarrow {}^{234}U$					$^{244}Cm(\alpha) \rightarrow {}^{240}Pu$					$^{237}Np(\alpha) \rightarrow {}^{233}Pa$	$^{233}Pa(\beta^-) \rightarrow {}^{233}U$		
Group	This work	Johnston [39]	Deviation (%)	Calculated	Deviation (%)	This work	Johnston [39]	Deviation (%)	Calculated	Deviation (%)	This work	This work	Calculated	Deviation (%)
Lι	0.2418 (29)	0.231 (3)	4.7 (19)	0.232 (8)	4.2 (38)	0.2306 (35)	0.214 (3)	7.8 (22)	0.219 (8)	5.3 (42)	1.472 (24)	1.075 (19)	1.05 (4)	2.4 (43)
Lα	3.816 (43)	3.81 (3)	0.2 (14)	3.73 (12)	2.3 (12)	3.49 (5)	3.38 (3)	3.3 (17)	3.42 (11)	2.0 (36)	22.64 (30)	15.69 (20)	16.9 (6)	-7.2 (35)
Lη	0.1284 (16)	0.126 (2)	1.9 (16)	0.118 (5)	8.8 (46)	0.1002 (22)	0.102 (2)	-1.8 (29)	0.092 (4)	9 (5)	0.545 (12)	0.235 (19)	0.272 (16)	-14 (9)
Lβ	5.23 (6)	5.18 (4)	1.0 (14)	5.23 (16)	0.0 (33)	4.22 (6)	4.08 (3)	3.4 (17)	4.21 (14)	0.2 (36)	25.43 (33)	16.89 (25)	18.1 (6)	-6.7 (34)
Lγ	1.291 (14)	1.29 (1)	0.1 (11)	1.23(4)	5.0 (36)	1.023 (15)	0.991 (8)	3.2 (17)	0.97 (4)	5.5 (46)	5.96 (8)	3.97 (6)	4.23 (14)	-6.1 (34)

Table 3. Absolute and relative individual L X-ray emission intensities, respectively per 100 decays and per 100 emitted L X-rays, of ^{238}Pu(α) → ^{234}U and ^{244}Cm(α) → ^{240}Pu. The L_3 X-rays have many satellites, therefore the given energy corresponds to the main component or to the energy range for Lu, Lβ_7, Lβ_5. u_i are the relative uncertainty contributions, u_1, u_2 and u_3 are respectively the contribution of the source activity and the live time, the contribution of the fitting processing and counting statistics, and the contribution of the FEP efficiency and the source inhomogeneity. u_1, u_2 and u_3 contribute to the combined uncertainty of absolute intensities per 100 decays, while only u_2 contributes to the uncertainty of the relative intensities per 100 L X-rays.

Line		^{238}Pu(α) → ^{234}U						^{244}Cm(α) → ^{240}Pu					
Siegbahn	IUPAC	Energy (eV)	X-ray emission intensity		Rel. Unc. (%)			Energy (eV)	X-ray emission intensity		Rel. Unc. (%)		
			per 100 L X-rays	per 100 decays	u_1	u_2	u_3		per 100 L X-rays[6]	per 100 decays	u_1	u_2	u_3
-	L_1-L_3	4589.2	0.0214 (44)	0.00229 (47)	0.72	20	1.2	5054.63	0.0267 (13)	0.00242 (13)	0.37	5.0	1.6
Lι	L_3-M_1	11618.4	2.257 (11)	0.2418 (30)	0.72	0.49	0.86	12124.4	2.540 (13)	0.2306 (36)	0.37	0.49	1.4
Ls	L_3-M_2	11982.0	0.0227 (15)	0.00243 (16)	0.72	6.6	0.86	12503	0.0269 (20)	0.00244 (18)	0.37	7.4	1.4
Lt	L_3-M_3	12864.7	0.0286 (17)	0.00307 (18)	0.72	5.8	0.86	13485.4	0.0315 (16)	0.00286 (15)	0.37	5.2	1.4
Lα_2	L_3-M_4	13439.8	3.604 (7)	0.3862 (44)	0.72	0.20	0.86	14074.5	3.806 (11)	0.346 (5)	0.37	0.29	1.4
Lα_1	L_3-M_5	13614.8	32.007 (20)	3.429 (39)	0.72	0.062	0.86	14237	34.68 (7)	3.149 (47)	0.37	0.21	1.4
Lη	L_2-M_1	15398.8	1.199 (6)	0.1284 (16)	0.72	0.50	0.86	16333.5	1.103 (18)	0.1002 (22)	0.37	1.6	1.4
Lβ_6	L_3-N_1	15726.1	0.593 (9)	0.0636 (12)	0.72	1.5	0.86	16497.9	0.635 (7)	0.0576 (11)	0.37	1.2	1.4
L$\beta_{2,15}$	L_3-$N_{4,5}$	16386.8 16539.6	7.626 (10)	0.817 (9)	0.721	0.129	0.858	17207.5 17411.8	8.271 (19)	0.751 (11)	0.37	0.23	1.4
Lβ_4	L_1-M_2	16575.0	0.2240 (29)	0.02400 (41)	0.72	1.3	0.86	17555.2	0.2506 (47)	0.0228 (5)	0.37	1.9	1.4
Lβ_{17}	L_2-M_3	16647.1	0.0681 (25)	0.00730 (28)	0.72	3.7	0.86	17702.8	0.0531 (13)	0.00482 (14)	0.37	2.5	1.4
Lu Lβ_7	L_3-$N_{6,7}$ L_3-O_1	16774.5 16974.0	0.257 (11)	0.0276 (12)	0.72	4.3	0.86	17629.1 17749.4	0.240 (8)	0.0218 (8)	0.37	3.5	1.4
Lβ_5	L_3-$O_{4,5}$ L_3-$P_{1,2,3}$	17064.0 17123.2	1.636 (31)	0.1753 (38)	0.72	1.87	0.86	17951.2 18072.4	1.725 (14)	0.1566 (26)	0.37	0.81	1.4

[6] Relative X-ray emission intensities from the ^{244}Cm decay have been published by our group in [51]. In this publication, a left tail component was applied to the intense peaks, these tails tend to unbalance the fit and to underestimate intensities of the transitions on the left side of the intense peaks. In the present work the data and spectrum processing were improved, no left tail has been introduced and the energy resolution was improved from 37 eV to 31 eV. In addition, the uncertainty contribution from the fitting processing is included in the present uncertainty budget.

Lβ_1	L_2-M_4	17220.2	38.19 (11)	4.091 (47)	0.72	0.28	0.86	18293.3	35.138 (34)	3.190 (47)	0.37	0.10	1.4
Lβ_3	L_1-M_3	17455.0	0.1933 (27)	0.02071 (37)	0.72	1.4	0.86	18541	0.1879 (27)	0.01706 (35)	0.37	1.4	1.4
Lβ_{10}	L_1-M_4	18029.3	0.01298 (31)	0.001390 (36)	0.72	2.4	0.86	19137	0.0045 (6)	0.00041 (6)	0.37	14	1.4
Lβ_9	L_1-M_5	18204.9	0.01711 (35)	0.001833 (43)	0.72	2.1	0.86	19330.3	0.0122 (8)	0.00111 (7)	0.37	6.5	1.4
Lγ_5	L_2-N_1	19506.4	0.3324 (45)	0.0356 (6)	0.72	1.3	0.86	20707.4	0.3154 (34)	0.0286 (5)	0.37	1.1	1.4
-	L_2-N_3	19901.0	0.0242 (16)	0.00259 (18)	0.72	6.7	0.86	21146.6	0.0242 (11)	0.00220 (10)	0.37	4.4	1.4
Lγ_1	L_2-N_4	20166.5	9.386 (8)	1.006 (11)	0.72	0.088	0.86	21416.8	8.683 (24)	0.788 (12)	0.27	0.27	0.3
Lγ_2	L_1-N_2	20482.0	0.0615 (10)	0.00659 (13)	0.72	1.7	0.86	21720.6	0.0705 (32)	0.00640 (31)	0.37	4.6	1.4
Lγ'_8	L_2-N_6	20556.1	0.0616 (8)	0.00660 (11)	0.72	1.3	0.86	21829.3	0.0607 (21)	0.00551 (21)	0.37	3.4	1.4
Lγ_8	L_2-O_1	20625.7	0.0910 (11)	0.00975 (16)	0.72	1.2	0.86	21914	0.0646 (18)	0.00586 (18)	0.37	2.8	1.4
Lγ_3	L_1-N_3	20712.4	0.0594 (13)	0.00636 (15)	0.72	2.1	0.86	21980	0.0665 (18)	0.00604 (18)	0.37	2.6	1.4
Lγ_6	L_2-O_4	20842.0	1.948 (6)	0.2087 (18)	0.72	0.33	0.36	22149.1	1.911 (9)	0.1735 (27)	0.37	0.45	1.4
-	L_2-P_1	20904.0	0.0117 (17)	0.00126 (18)	0.72	15	0.86	-	-	-	-	-	-
-	L_2-$P_{4,5}$	20941.7	0.03312 (50)	0.00355 (7)	0.72	1.5	0.86	22260.9	0.0343 (11)	0.00312 (11)	0.37	3.2	1.4
Lγ'_4	L_1-O_2	21498.1	0.01838 (41)	0.001969 (49)	0.72	2.2	0.85	22823.3	0.0141 (7)	0.00128 (7)	0.37	5.0	1.4
Lγ_4	L_1-O_3	21564.0	0.01345 (34)	0.001441 (39)	0.72	2.5	0.85	22888.8	0.0162 (8)	0.00147 (7)	0.37	4.6	1.4
-	L_1-P_2	21736.6	0.00561 (27)	0.000601 (30)	0.72	4.9	0.85	23082.1	0.0059 (5)	0.000537 (46)	0.37	8.5	1.4

Table 4. Comparison between some individual L X-ray emission intensities per 100 decays of $^{238}Pu(\alpha) \rightarrow {}^{234}U$ obtained in this work with those measured by either Johnston and Burns [39] or Dryak et al. [38].

Siegbahn	**IUPAC**	**This work** I_W **(%)**	**Dryak** [38] I_D **(%)**	**Deviation** $(I_W-I_D)/I_D$ **(%)**	**Johnston** [39] I_W **(%)**	**Deviation** $(I_w-I_J)/I_J$ **(%)**
Lι	L_3-M_1	0.2418 (30)	0.240 (10)	0.7 (44)	0.2310 (30)	4.7 (19)
Lt	L_3-M_2	0.00243 (16)	0.00310 (30)	-22 (9)	-	-
Ls	L_3-M_3	0.00307 (18)	0.00280 (30)	10 (13)	-	-
Lα_2	L_3-M_4	0.3862 (44)	0.400 (40)	-3 (10)	-	-
Lα_1	L_3-M_5	3.429 (39)	3.50 (11)	-2.0 (33)	-	-
Lη	L_2-M_1	0.1284 (16)	0.127 (5)	1.1 (42)	0.1260 (20)	1.9 (21)
Lβ_6	L_3-N_1	0.0636 (12)	0.063 (6)	1 (10)	0.0620 (20)	2.6 (38)
L$\beta_{2,15}$	L_3-$N_{4,5}$	0.817 (9)	0.740 (30)	10.4 (46)	0.822 (7)	-0.6 (14)
Lβ_1	L_2-M_4	4.091 (47)	4.04 (14)	1.3 (37)	4.260 (40)	-4.0 (14)
Lβ_3	L_1-M_3	0.02071 (37)	0.0260 (30)	-20 (9)	0.0250 (10)	-17.2 (36)
Lβ_{10}	L_1-M_4	0.001390 (36)	-	-	0.00510 (20)	-72.7 (13)
Lβ_9	L_1-M_5	0.001833 (43)	-	-	0.00260 (20)	-30 (6)
Lγ_5	L_2-N_1	0.0356 (6)	0.0310 (10)	14.8 (42)	0.0360 (20)	-1 (6)
Lγ_1	L_2-N_4	1.006 (11)	0.920 (30)	9.3 (38)	0.992 (7)	1.4 (13)
Lγ_8	L_2-O_1	0.00975 (16)	-	-	0.0262 (6)	-62.8 (10)
Lγ_6	L_2-O_4	0.2087 (18)	0.194 (11)	8 (6)	0.2280 (30)	-8.5 (14)
Lγ'_4	L_1-O_2	0.001969 (49)	0.00200 (20)	-2 (10)	0.00360 (10)	-45.3 (20)
Lγ_4	L_1-O_3	0.001441 (39)	0.00200 (20)	-28 (7)	-	-
Lγ_{13}	L_1-P_2	6.01 (30) E-04	-	-	9.0 (10) E-04	-33 (8)

Table 5. Absolute and relative individual L X-ray emission intensities respectively per 100 decays and per 100 emitted L X-rays of $^{237}Np(\alpha) \rightarrow {}^{233}Pa$ and $^{233}Pa(\beta^-) \rightarrow {}^{233}U$,. u_i are the relative uncertainty contributions, u_1, u_2 and u_3 are respectively the contribution of the source activity and the live time, the contribution of the fitting processing and counting statistics, and the contribution of the FEP efficiency and the source inhomogeneity. u_1, u_2 and u_3 contribute to the combined uncertainty of absolute intensities per 100 decays, while only u_2 contributes to the uncertainty of the relative intensities per 100 L X-rays.

Line		$^{237}Np(\alpha) \rightarrow {}^{233}Pa$						$^{233}Pa(\beta^-) \rightarrow {}^{233}U$					
Siegbahn	IUPAC	Energies	X-ray emission intensity		Rel. Unc. (%)			Energies	X-ray emission intensity		Rel. Unc. (%)		
		(eV)	per 100 L X-rays	per 100 decays	u_1	u_2	u_3	(eV)	per 100 L X-rays	per 100 decays	u_1	u_2	u_3
-	L_1-L_3	-	-	-	-	-	-	4590	0.744 (32)	0.284 (13)	0.68	4.4	1.3
$L\iota$	L_3-M_1	11367.9	2.626 (27)	1.472 (24)	0.68	1.0	1.1	11618.4	2.819 (34)	1.075 (19)	0.68	1.2	1.1
$L\alpha_2$	L_3-M_4	13121.8	4.183 (34)	2.345 (41)	0.68	1.2	1.1	13439.8	4.244 (41)	1.619 (26)	0.68	1.0	1.1
$L\alpha_1$	L_3-M_5	13289.5	36.21 (10)	20.30 (27)	0.68	0.34	1.1	13616.5	36.88 (15)	14.07 (19)	0.68	0.39	1.1
$L\eta$	L_2-M_1	14949.0	0.972 (16)	0.545 (12)	0.68	1.8	1.1	15398.8	0.615 (48)	0.235 (19)	0.68	7.9	0.9
$L\beta_6$	L_3-N_1	15349.9	0.675 (14)	0.378 (19)	0.68	4.8	1.3	15726.1	0.851 (18)	0.325 (8)	0.68	2.2	1.1
$L\beta_{2,15}$	L_3-$N_{4.5}$	15990.0	7.995 (46)	4.48 (13)	0.68	2.5	1.0	16426.6	8.63 (32)	3.29 (13)	0.68	3.7	1.2
$L\beta_4$	L_1-M_2	16104.1	2.236 (25)	1.253 (21)	0.68	1.1	1.1	16574.4	5.7 (6)	2.18 (23)	0.68	10	0.8
$L\beta_7$	L_3-O_1	16428	0.139 (6)	0.0781 (36)	0.68	4.5	1.1	-	-	-	-	-	-
Lu, $L\beta_7$	L_3-$N_{6,7}$ L_3-O_1	-	-	-	-	-	-	16844.0	0.226 (27)	0.086 (10)	0.68	11.8	1.8
$L\beta_5$	L_3-$O_{4.5}$	16636.0	1.625 (21)	0.91 (6)	0.68	7.0	1.4	17075.2	1.74 (7)	0.662 (27)	0.68	3.9	1.0
$L\beta_1$	L_2-M_4	16704.0	31.44 (9)	17.62 (23)	0.68	0.29	1.1	17219.8	21.32 (9)	8.13 (11)	0.68	0.4	1.1
$L\beta_3$	L_1-M_3	16932.7	1.258 (18)	0.705 (16)	0.68	1.9	1.0	17454.8	4.809 (49)	1.834 (30)	0.68	1.0	1.1
$L\beta_{10}$	L_1-M_4	-	-	-	-	-	-	18028.1	0.286 (11)	0.1091 (43)	0.68	3.8	1.1
$L\beta_9$	L_1-M_5	-	-	-	-	-	-	18206.7	0.453 (29)	0.173 (11)	0.68	6.3	0.9
$L\gamma_5$	L_2-N_1	18931.0	0.251 (8)	0.140 (5)	0.68	3.3	1.1	19507.0	0.26 (5)	0.098 (21)	0.68	21	3.9
$L\gamma_1$	L_2-N_4	19565.7	7.385 (45)	4.14 (6)	0.68	0.7	1.1	20168.0	5.16 (6)	1.970 (34)	0.68	1.1	1.1
$L\gamma_2$	L_1-N_2	19889.7	0.384 (10)	0.215 (8)	0.68	3.7	1.0	20484.6	1.736 (30)	0.662 (14)	0.68	1.7	1.1

Lγ_3	L_1-N_3	20101.1	0.408 (11)	0.229 (7)	0.68	2.6	1.1	-	-	-	-	-	-
Lγ'_8	L_2-N_6	-	-	-	-	-	-	20556.1	0.121 (7)	0.0461 (29)	0.68	6.0	1.0
Lγ_8	L_2-O_1	-	-	-	-	-	-	20625.7	0.152 (12)	0.0581 (48)	0.68	8.2	1.4
Lγ_3	L_1-N_3	-	-	-	-	-	-	20713.3	1.308 (32)	0.499 (14)	0.68	2.4	1.0
Lγ_6	L_2-O_4	20217.0	1.550 (20)	0.869 (22)	0.68	2.2	1.2	20842.7	1.016 (23)	0.387 (10)	0.68	2.3	1.0
Lγ_4	L_1-$O_{2.3}$	20860.0 20917.0	0.371 (10)	0.208 (7)	0.68	3.0	1.1	21498.0 21564.0	0.763 (18)	0.291 (8)	0.68	2.3	1.1
-	L_1-$O_{4,5}$ L_1-$P_{2,3}$	21006.0	0.116 (6)	0.0648 (39)	0.68	5.9	1.0	21736.6	0.143 (8)	0.0545 (32)	0.68	5.8	1.2

References

[1] P.W. Durbin, Metabolism and Biological Effects of the Transplutonium Elements, in: H.C. Hodge, J.B. Hursh, J.N. Stannard (Eds.), Uranium · Plutonium Transplutonic Elem., Springer Berlin Heidelberg, Berlin, Heidelberg, 1973: pp. 739–896. https://doi.org/10.1007/978-3-642-65551-7_18.

[2] N. Vajda, C.-K. Kim, Determination of Transuranium Isotopes (Pu, Np, Am) by Radiometric Techniques: A Review of Analytical Methodology, Anal. Chem. 83 (2011) 4688–4719. https://doi.org/10.1021/ac2008288.

[3] K. Mayer, M. Wallenius, I. Ray, Nuclear forensics—a methodology providing clues on the origin of illicitly trafficked nuclear materials, The Analyst. 130 (2005) 433–441. https://doi.org/10.1039/B412922A.

[4] S. Abousahl, P. van Belle, H. Eberle, H. Ottmar, B. Lynch, P. Vallet, K. Mayer, M. Ougier, Development of quantitative analytical methods for the control of actinides in a pyrochemical partitioning process, Radiochim. Acta. 93 (2005). https://doi.org/10.1524/ract.93.3.147.61614.

[5] D. Reilly, N. Ensslin, H. Smith, S. Kreiner, Los Alamos National Laboratory (U.S.), Etats-Unis, Nuclear Regulatory Commission, Passive nondestructive assay of nuclear materials, US Department of Commerce, National Technical Information Service, Springfield, VA, 1991.

[6] NEA/NSC/WPNCS/DOC(2011)5, Spent Nuclear Fuel Assay Data for Isotopic Validation - State-of-the-art Report, OECD, Paris, 2011.

[7] H. Nitsche, R.C. Gatti, Sh.C. Lee, Low-level determination of plutonium by gamma and L X-ray spectroscopy, J. Radioanal. Nucl. Chem. Artic. 161 (1992) 401–411. https://doi.org/10.1007/BF02040486.

[8] D. Arnold, W. Kolb, Determination of plutonium content and isotopic ratios in environmental samples by L x-ray and α-particle measurements, Appl. Radiat. Isot. 46 (1995) 1151–1157. https://doi.org/10.1016/0969-8043(95)00158-A.

[9] M.-M. Bé, V. Chisté, X. Mougeot, V.P. Chechev, F.G. Kondev, A.L. Nichols, X. Huang, B. Wang, Table of radionuclides. Vol. 7: A=14 to 245, BIPM, Sèvres, 2013.

[10] C. Dulieu, M.A. Kellett, X. Mougeot, Dissemination and visualisation of reference decay data from Decay Data Evaluation Project (DDEP), EPJ Web Conf. 146 (2017) 07004. https://doi.org/10.1051/epjconf/201714607004.

[11] E. Schönfeld, H. Janßen, Calculation of emission probabilities of X-rays and Auger electrons emitted in radioactive disintegration processes, Appl. Radiat. Isot. 52 (2000) 595–600. https://doi.org/10.1016/S0969-8043(99)00216-X.

[12] J. Plagnard, C. Bobin, M.-C. Lépy, Accurate efficiency calibration of a low-energy HPGe detector using a monochromatic x-ray source, X-Ray Spectrom. 36 (2007) 191–198. https://doi.org/10.1002/xrs.961.

[13] J.L. Campbell, P.L. McGhee, State-of-the-art efficiency determination for a Si(Li) X-ray detector in the 3–40 keV energy range, Nucl. Instrum. Methods Phys. Res. Sect. Accel. Spectrometers Detect. Assoc. Equip. 248 (1986) 393–404. https://doi.org/10.1016/0168-9002(86)91024-7.

[14] J.L. Campbell, report prepared for the International Initiative on X-ray Fundamental Parameters, in: Paris, 2014.

[15] V.M. Gorozhankin, M.-M. Bé, Assessment of internal conversion coefficients for anomalous electric dipole transitions, Appl. Radiat. Isot. 66 (2008) 722–728. https://doi.org/10.1016/j.apradiso.2008.02.077.

[16] T. Sikorsky, J. Geist, D. Hengstler, S. Kempf, L. Gastaldo, C. Enss, C. Mokry, J. Runke, C.E. Düllmann, P. Wobrauschek, K. Beeks, V. Rosecker, J.H. Sterba, G. Kazakov, T. Schumm, A. Fleischmann, Measurement of the Th 229 Isomer Energy with a Magnetic Microcalorimeter, Phys. Rev. Lett. 125 (2020) 142503. https://doi.org/10.1103/PhysRevLett.125.142503.

[17] A. Fleischmann, C. Enss, G.M. Seidel, Metallic Magnetic Calorimeters, in: C. Enss (Ed.), Cryog. Part. Detect., Springer Berlin Heidelberg, Berlin, Heidelberg, 2005: pp. 151–216. https://doi.org/10.1007/10933596_4.

[18] M. Rodrigues, R. Mariam, M. Loidl, A metallic magnetic calorimeter dedicated to the spectrometry of L X-rays emitted by actinides,

EPJ Web Conf. 146 (2017) 10012. https://doi.org/10.1051/epjconf/201714610012.
[19] M. Rodrigues, M. Loidl, C. Le-Bret, A Novel Type of Absorber Presenting a Constant Detection Efficiency for up to 25 keV X-Ray Photons, J. Low Temp. Phys. 167 (2012) 510–515. https://doi.org/10.1007/s10909-012-0537-3.
[20] A. Burck, S. Kempf, S. Schäfer, H. Rotzinger, M. Rodrigues, T. Wolf, L. Gastaldo, A. Fleischmann, C. Enss, Microstructured Magnetic Calorimeter with Meander-Shaped Pickup Coil, J. Low Temp. Phys. 151 (2008) 337–344. https://doi.org/10.1007/s10909-007-9659-4.
[21] K. Debertin, R.G. Helmer, Gamma- and x-ray spectrometry with semiconductor detectors, North-Holland ; Sole distributors for the USA and Canada, Elsevier Science Pub. Co, Amsterdam ; New York : New York, NY, USA, 1988.
[22] R. Mariam, M. Rodrigues, M. Loidl, Full-Energy Peak Efficiency Calibration of a Metallic Magnetic Calorimeter Detector for Photon Spectrometry Below 100 keV, J. Low Temp. Phys. 193 (2018) 1269–1275. https://doi.org/10.1007/s10909-018-2001-5.
[23] C. Agarwal, S. Chaudhury, A. Goswami, M. Gathibandhe, Full energy peak efficiency calibration of HPGe detector for point and extended sources using Monte Carlo code, J. Radioanal. Nucl. Chem. 287 (2011) 701–708. https://doi.org/10.1007/s10967-010-0820-1.
[24] Y. Ménesguen, M. Gerlach, B. Pollakowski, R. Unterumsberger, M. Haschke, B. Beckhoff, M.-C. Lépy, High accuracy experimental determination of copper and zinc mass attenuation coefficients in the 100 eV to 30 keV photon energy range, Metrologia. 53 (2016) 7–17. https://doi.org/10.1088/0026-1394/53/1/7.
[25] S. Pommé, Typical uncertainties in alpha-particle spectrometry, Metrologia. 52 (2015) S146–S155. https://doi.org/10.1088/0026-1394/52/3/S146.
[26] D. McCammon, Thermal Equilibrium Calorimeters – An Introduction, in: C. Enss (Ed.), Cryog. Part. Detect., Springer Berlin Heidelberg, Berlin, Heidelberg, 2005: pp. 1–34. https://doi.org/10.1007/10933596_1.
[27] J. Bouchard, MTR2: a discriminator and dead-time module used in counting systems, Appl. Radiat. Isot. 52 (2000) 441–446. https://doi.org/10.1016/S0969-8043(99)00192-X.
[28] H. Ruellan, M.C. Lépy, M. Etcheverry, J. Plagnard, J. Morel, A new spectra processing code applied to the analysis of 235U and 238U in the 60 to 200 keV energy range, Nucl. Instrum. Methods Phys. Res. Sect. Accel. Spectrometers Detect. Assoc. Equip. 369 (1996) 651–656. https://doi.org/10.1016/S0168-9002(96)80070-2.
[29] J.L. Campbell, T. Papp, WIDTHS OF THE ATOMIC K–N7 LEVELS, At. Data Nucl. Data Tables. 77 (2001) 1–56. https://doi.org/10.1006/adnd.2000.0848.
[30] J. Hoszowska, J.-Cl. Dousse, Ch. Rhême, Linewidths of photoinduced *L* x rays of uranium, Phys. Rev. A. 50 (1994) 123–131. https://doi.org/10.1103/PhysRevA.50.123.
[31] F.T. Porter, M.S. Freedman, Recommended atomic electron binding energies, 1 *s* to 6 $p_{3/2}$, for the heavy elements, *Z* =84 to 103, J. Phys. Chem. Ref. Data. 7 (1978) 1267–1284. https://doi.org/10.1063/1.555584.
[32] J.H. Scofield, Hartree-Fock values of L x-ray emission rates, Phys. Rev. A. 10 (1974) 1507–1510. https://doi.org/10.1103/PhysRevA.10.1507.
[33] J.L. Campbell, Fluorescence yields and Coster–Kronig probabilities for the atomic L subshells. Part II: The L1 subshell revisited, At. Data Nucl. Data Tables. 95 (2009) 115–124. https://doi.org/10.1016/j.adt.2008.08.002.
[34] F. Parente, M.H. Chen, B. Crasemann, H. Mark, L x-ray satellite energies, At. Data Nucl. Data Tables. 26 (1981) 383–466. https://doi.org/10.1016/0092-640X(81)90013-9.
[35] N. Imanishi, F. Ichiro, Double Vacancy Formation in L Shell Accompanying the Internal Conversion of ^{234}U 43. 48 keV Transition, Bull. Inst. Chem. Res. (1982) 140–146.
[36] E. García-Toraño, T. Durán Ramiro, C. Burgos, M. Begoña Ahedo, Defined solid-angle counter with variable geometry, Appl. Radiat. Isot. 66 (2008) 881–885. https://doi.org/10.1016/j.apradiso.2008.02.040.
[37] M.A. Kellett, O. Bersillon, The Decay Data Evaluation Project (DDEP) and the JEFF-3.3 radioactive decay data library: Combining international collaborative efforts on evaluated

decay data, EPJ Web Conf. 146 (2017) 02009. https://doi.org/10.1051/epjconf/201714602009.
[38] Dryak P, Egorov Yu S, Nedovesov V G, Plkh I, Shukin G E, Proc. 34th Ann. Conf. Nucl. Spectrosc. At. Nuclei, Alma-Ata, in: 1984: p. 540.
[39] P.N. Johnston, P.A. Burns, Absolute L X-ray intensities in the decays of 230Th, 234U, 238Pu and 244Cm, Nucl. Instrum. Methods Phys. Res. Sect. Accel. Spectrometers Detect. Assoc. Equip. 361 (1995) 229–239. https://doi.org/10.1016/0168-9002(95)00043-7.
[40] J. Byrne, W. Gelletly, M.A.S. Ross, F. Shaikh, L 2 - Subshell Yield Measurements in Pu 240 , U 236 , and U 234, Phys. Rev. 170 (1968) 80–90. https://doi.org/10.1103/PhysRev.170.80.
[41] Bemis, Jr. C.E, Tubbs, L., Absolute L-Series X-Ray and Low-Energy Gamma-Ray Yields for Most Transuranium Nuclide, in: Oak Ridge National Laboratory, 1977: pp. 93–94.
[42] S. Seltzer, XCOM-Photon Cross Sections Database, NIST Standard Reference Database 8, (1987). https://doi.org/10.18434/T48G6X.
[43] J.H. Scofield, Relativistic hartree-slater values for K and L X-ray emission rates, At. Data Nucl. Data Tables. 14 (1974) 121–137. https://doi.org/10.1016/S0092-640X(74)80019-7.
[44] I.M. Lowles, T.D. Mac Mahon, M.F. Banham, A.J. Fudge, R.A.P. Wiltshire, Reconciliation of 237Np decay scheme data, Nucl. Instrum. Methods Phys. Res. Sect. Accel. Spectrometers Detect. Assoc. Equip. 286 (1990) 556–562. https://doi.org/10.1016/0168-9002(90)90916-T.
[45] G. Shchukin, K. Iakovlev, J. Morel, Analysis of the 237Np–233Pa photon spectrum using the full response function method, Appl. Radiat. Isot. 60 (2004) 239–246. https://doi.org/10.1016/j.apradiso.2003.11.024.
[46] D. DeVries, H. Griffin, X- and -ray emissions observed in the decay of 237Np and 233Pa, Appl. Radiat. Isot. 66 (2008) 668–675. https://doi.org/10.1016/j.apradiso.2007.07.019.
[47] U. Schötzig, E. Schönfeld, H. Janszen, Standardization and photon emission probabilities in the decay of 237Np/233Pa, Appl. Radiat. Isot. 52 (2000) 883–889. https://doi.org/10.1016/S0969-8043(99)00137-2.
[48] V.P. Chechev, N.K. Kuzmenko, Decay Data Evaluation Project (DDEP): Evaluation of the main 233Pa decay characteristics, Appl. Radiat. Isot. 64 (2006) 1403–1411. https://doi.org/10.1016/j.apradiso.2006.02.053.
[49] S. Puri, D. Mehta, B. Chand, N. Singh, P.N. Trehan, L shell fluorescence yields and coster—kronig transition probabilities for the elements with 25 < Z < 96, X-Ray Spectrom. 22 (1993) 358–361. https://doi.org/10.1002/xrs.1300220507.
[50] J.L. Campbell, Fluorescence yields and Coster–Kronig probabilities for the atomic L subshells. Part II: The L1 subshell revisited, At. Data Nucl. Data Tables. 95 (2009) 115–124. https://doi.org/10.1016/j.adt.2008.08.002.
[51] R. Mariam, M. Rodrigues, M. Loidl, Determination of L-X-ray line emission intensities in the decay of Cm-244 with a metallic magnetic calorimeter, Nucl. Instrum. Methods Phys. Res. Sect. Accel. Spectrometers Detect. Assoc. Equip. 954 (2020) 162066. https://doi.org/10.1016/j.nima.2019.04.020.